

Semiconducting Black Phosphorus

A. Morita

Department of Physics, Tohoku University, Sendai, 980 Japan

Received 1 October 1985/Accepted 8 December 1985

Abstract. Black phosphorus is a narrow-gap semiconductor newly attracting attention because of recent success in growing single crystals at a high temperature under a high pressure. **This review covers recent research work on the preparation, the crystal structure, the band structure, the electrical and optical properties, and the superconductivity of black phosphorus.**

PACS: 61, 71, 72, 74, 78

Though As, Sb, and Bi of the V_b group of the periodic table crystalize in semimetallic rhombohedral arsenic (A7) structure phase usually, phosphorus has a number of allotropic modifications [1] and its most stable form is black phosphorus (abbreviated as black-P hereafter). Black-P has a layered structure with an orthorhombic symmetry and has been known as an elemental narrow-gaped and p-type semiconductor with gap energy of about 0.3 eV from investigations on polycrystalline samples [2–4].

High-pressure measurement by Bridgeman [5], Jamieson [6] and others disclosed that black-P shows an interesting sequence of structural phase transformations from the semiconducting orthorhombic phase to the semimetallic rhombohedral (A7) phase at about 5 GPa and to the metallic simple cubic phase at about 10 GPa. The existence of the metallic simple cubic phase, which is a rather low packing structure, under high pressure is noticeable. The only other example of the simple cubic phase is that of Po [1].

It is known that the metallic simple cubic phase shows superconductivity with T_c of about 6 K. Recently, Kawamura et al. [7] have disclosed that by cooling it down to liquid-He temperature first and then applying high pressure, black-P shows superconductivity with T_c even higher than 10 K.

In spite of these attractive properties, theoretical and experimental studies of black-P until recently remained in a rather immature stage because of the difficulty in growing a large single crystal. In 1978 theoretical studies of the band structure and the

structural stability of black-P were initiated [8, 9] and, in succession, a couple of groups in Japan have succeeded in growing large single crystals from red phosphorus melt at a high temperature and cooled slowly under a high pressure using a wedge-type cubic anvil apparatus [10, 11]. This success has made it possible to study its electrical and optical properties extensively.

Before then detailed studies of elemental semiconductors had seemed to be confined to Te and Se besides Si, Ge, and Sn. As investigations on black-P by using single crystals progressed, however, many interesting and unique properties of this substance different from other elemental semiconductors have been discovered.

The aim of this review is to cover recent progress in theoretical and experimental studies on black-P. In the next section the preparation of single crystals is described briefly. In Sect. 2 the crystal structures at normal condition and also at high pressures are presented. Section 3 is devoted to describing the band structure and dielectric functions calculated in terms of the self-consistent pseudopotential method. Section 4 is devoted to discussion of the optical properties of black-P: photoelectron spectroscopy, optical properties due to electronic excitation and those due to phonon excitation. In Sect. 5 semiconducting properties such as the cyclotron resonance, electrical conduction and carrier mobilities, and the pressure effect on the band structure are discussed. Finally the superconductivity in black-P under high pressure is discussed in Sect. 6.

1. Preparation of Single Crystals

Black-P was produced for the first time by Bridgeman [5] in 1914 under the high pressure of 1.2 GPa at 200 °C. Using Bridgeman's method, in 1953, Keyes [2] produced black-P from white phosphorus in a high-pressure apparatus under the hydrostatic pressure of 1.3 GPa at 200 °C. He reported that after several minutes at this temperature the transition to black-P took place abruptly, accompanied by a marked change in volume (0.18 cm³/gr). The ingot of black-P was washed in carbon disulfide to remove any untransformed white phosphorus. As a result of the large volume change and the violent nature of the transition, the ingot was polycrystalline and contained numerous cracks. Grain sizes were roughly 0.1 mm diameter. When black-P was melted or vaporized, P₄ molecules were formed which crystallized into white or red phosphorus at normal pressure; thus it did not appear possible to prepare single-crystal samples.

In the course of studying the polymorphism of phosphorus, it was found that black-P can be prepared in a well-crystallized condition, though very tiny needle-shaped, from solution of phosphorus in liquid bismuth [12]. Maruyama et al. [4] poured melted bismuth onto white phosphorus, which was purified by washing with 15% HNO₃ and water-steam distillation successively. It was well shaken and the mixture (solution) was then kept at 400 °C for 20 h and cooled slowly (ca. 0.3 °C/min) to room temperature. Dissolving solid bismuth with 30% HNO₃, they obtained needle- or thin rod-like black-P single crystals from the residual solution. The size of a typical crystal was of 5 × 0.1 × 0.07 mm³ (needle direction: a axis).

In 1981, Shirotni et al. [10] succeeded for the first time in growing large single crystals of black-P (4 × 2 × 0.2 mm³) from red phosphorus melted at a high temperature under a high pressure using a wedge-type cubic high-pressure apparatus. They observed that under the high pressure of 3.8 GPa samples grown at 200 °C were amorphous-like, but samples grown at a temperature higher than 270 °C were crystallized in a single crystal.

In 1982, Narita's group [11] obtained single crystals larger than 5 × 5 × 10 mm³ using a multianvil apparatus. To grow such large single crystals, first they converted red phosphorus powder into black-P under the high pressure of 1.0 GPa at about 550 °C, melted it at about 900 °C, and decreased the temperature slowly at the rate of 0.5 °C/min down to about 600 °C.

A single crystal of black-P can easily be peeled off into thin mica-like sheets with the ac plane as a cleaved surface. The cleaved surface shows metallic luster tinged with black.

All single crystals obtained by the methods mentioned previously are of p-type. However, Narita's group have succeeded in growing n-type samples by doping Te as donor impurity atoms in the process of growing single crystal [13].

2. Crystal Structure

2.1. At Normal Condition

The crystal structure of black-P at normal condition is orthorhombic and consists of puckered layers parallel to the ac plane. A single puckered layer is shown in Fig. 1. In what follows, for the sake of convenience, we take the axes of the Cartesian coordinates *x*, *y*, and *z* in the direction of the crystal axes *c*, *a*, and *b*, respectively. In a single puckered layer each atom is bonded with three neighboring atoms by covalent bonds, whose lengths are nearly equal to each other and the bond angles are close to a right angle, as shown in Table 1. These facts mean that the three covalent bonds are mainly made of 3*p* orbitals. Since the intralayer

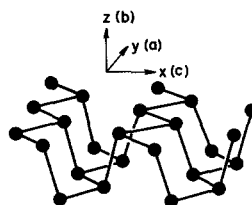


Fig. 1. A part of an infinite single-puckered layer of black-P

Table 1. Crystal structural parameters of black-P under the normal condition (numbers in parentheses are taken from [12] and otherwise from [15]). Note that the definition of *d*₁ and *d*₂ is the reverse of [12]

<i>a</i>	3.3133 Å (3.3136 Å)	lattice constants in orthorhombic system
<i>b</i>	10.473 Å (10.478 Å)	
<i>c</i>	4.374 Å (4.3763 Å)	
<i>u</i>	0.0806 (0.8056)	crystal structural parameters
<i>v</i>	0.1034 (0.10168)	
<i>d</i> ₁	2.222 Å (2.224 Å)	bond length
<i>d</i> ₂	2.277 Å (2.244 Å)	
<i>α</i> ₁	96.5° (96.34°)	bond angle between <i>d</i> ₁ s
<i>α</i> ₂	101.9° (102.09°)	bond angle between <i>d</i> ₁ and <i>d</i> ₂

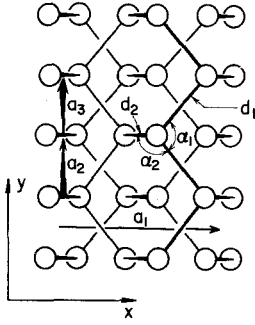


Fig. 2. The projection of two adjacent puckered layers on the xy plane. Bond lengths d_1 and d_2 , bond angles α_1 and α_2 and primitive translation vectors a_1 , a_2 , and a_3 are shown

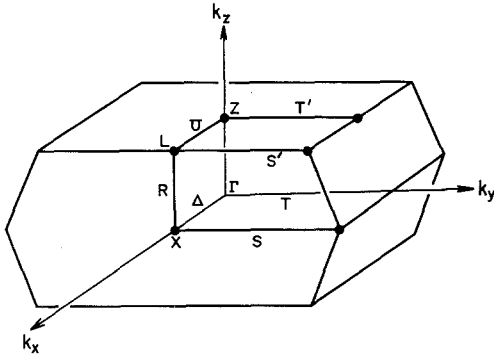


Fig. 3. The Brillouin zone of black-P

interatomic interactions are saturated chemically, intralayer interactions are van der Waals-like.

The projection of two neighboring layers on the xy plane is shown in Fig. 2. The primitive translation vector, a_1 , a_2 , and a_3 , is given by

$$\begin{aligned} a_1 &= c\hat{x}, & a_2 &= (a/2)\hat{y} - (b/2)\hat{z}, \\ a_3 &= (a/2)\hat{y} + (b/2)\hat{z}. \end{aligned} \quad (1)$$

The positions of four atoms in the primitive cell located at the origin are expressed, with the structural parameters u and v , by

$$\pm(uc, 0, vb), \quad 1/2(c, 0, b) \pm (uc, 0, -vb). \quad (2)$$

Values of the crystal axes, a , b , and c , and of the structural parameters, u and v , are given in Table 1. The space group of the structure is D_{2h}^{18} . The irreducible representations and the comprehensive relations with respect to the space group were given in [14].

Figure 3 shows the Brillouin zone. For reasons of symmetry any levels in the single group representation on the hexagonal surface and on the line V are doubly degenerate.

2.2. Under High Pressure

An appreciable anisotropy is observed among the compressibilities along the crystal axes; lattice parameters b and c decrease with increasing pressure, while

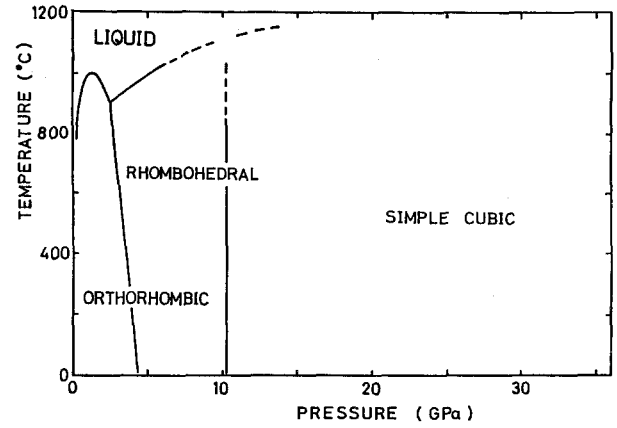


Fig. 4. Pressure vs. temperature phase diagram of black-P [18]

the lattice parameter a remains almost unchanged. The compressibility along the b axis is nearly the same as the one along the c axis up to a pressure of 2.7 GPa and, beyond that, it decreases gradually while that along the axis c remains almost constant [15, 16]. The average linear compressibilities between zero and 2.66 GPa are $K_a = 0.7$, $K_b = 119$, and $K_c = 124 \times 10^{-4} \text{ GPa}^{-1}$.

The unusual smallness of K_a indicates that the bond length and angle, d_1 and α_1 , of the zig-zag bond chain remain almost unchanged under pressure. The behavior of the lattice parameter b can be explained by a decrease in the interlayer van der Waals' gap under pressure. That of the lattice parameter c can be attributed to a decrease of the bond angle α_2 without any practical change of the bond length d_2 [17].

The transition from the orthorhombic to the rhombohedral phase at room temperature takes place at 5.5 ± 0.5 GPa. It is of the reconstruction type accompanied by the displacement of alternate puckered layers by $(a_2 + a_3)/2$ and a volume change, and takes place sluggishly when the temperature is below 400 °C.

The transition from the rhombohedral to the simple cubic phase takes place at 10.0 ± 0.6 GPa. It is accompanied by a volume change, though it is of the displacive type. The volume change decreases with increasing temperature and the transition becomes nearly of second order at temperatures higher than 700 °C. The transition pressure is almost independent of temperature [18]. It is noticeable that the simple cubic phase exists stably even at the high pressure of 60 GPa [19]. The pressure-temperature phase diagram of phosphorus which was determined by using the data obtained by a gasketed diamond anvil cell and a multianvil type x-ray system (MAX 80) designed for use of synchrotron orbital radiation (SOR) at high pressures and high temperatures in the Nat. Lab. for high energy physics at Tsukuba is shown in Fig. 4 [18].

3. Band Structure

The band structure of black-P was calculated using the tight-binding method [20], the self-consistent pseudopotential method [21] and the local-orbital method [21a]. The energy band and the density of states (DOS) obtained in [21] are shown in Fig. 5. A notable difference of the band structure of [21a] from that of [21] is the nature of the fundamental gap. That of [21a] is an indirect gap from the valence-band maximum at Z to the conduction-band maximum at Γ , while that of [20, 21] is direct at Z (Fig. 5). Measurement of optical spectra near the absorption threshold, which will be discussed later in Sect. 4.2, show that it is direct. The general features of the band structure can be understood in the following way.

First let us consider a single layer of black-P in which each atom is bound to three neighboring atoms by covalent bonds essentially made of 3p orbitals. In the two-dimensional band structure of the single layer, therefore, the upper part of the valence bands consists of the bonding 3p levels and the lower part of the conduction bands of the anti-bonding 3p levels (Fig. 6c). According to the tight-binding calculation [20], the energy gap between them is found to be located at the point Γ , with a value of about 2.5 eV. Wave functions at the top of the valence band and the bottom of the conduction band are mostly p_z -like. This fact means that levels near the gap are related to the bonds d_2 bridging the zig-zag bond-chains running along the y direction.

The tight-binding calculation also shows that the separation between the bonding and anti-bonding levels related to the bonds d_1 , which consist of mainly $3p_x$ and $3p_y$ orbitals, is larger than the energy gap at Γ associated with the bonds d_2 . This situation is shown

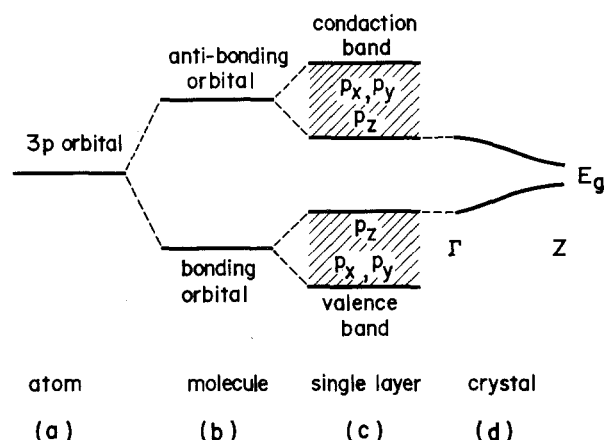


Fig. 6a-d. Schematic energy-level diagrams of phosphorus 3p orbital in (a) atom, (b) molecule, (c) single puckered layer, and (d) black phosphorus. In the case of (d), the top of the valence band and the bottom of the conduction band along the line $\Gamma-Z$ are shown

schematically in Fig. 6c. This explains the reason why the bond d_1 is stiffer than the bond d_2 , as was seen in the previous section.

In the three-dimensional black-P, the discussion based on the tight-binding calculation [20] tells us that interlayer interactions cause an upward dispersion to the top of the valence band and a downward one to the bottom of the conduction band along the $\Gamma-Z$ line. They give rise to the direct minimum gap of about 0.3 eV at the point Z (Fig. 6d). Thus black-P has a single valley for a hole and a single valley for an electron at the point Z.

At this point it is interesting to consider the pressure dependence of the gap. According to the above-mentioned discussion, the decrease of the interlayer

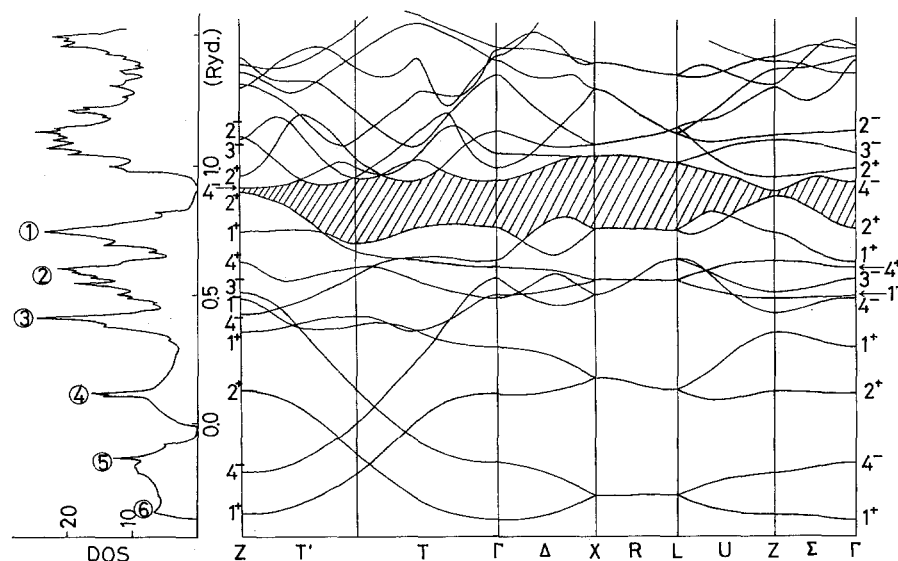


Fig. 5. The energy bands and the density of states of black-P calculated by the self-consistent pseudopotential method [21]

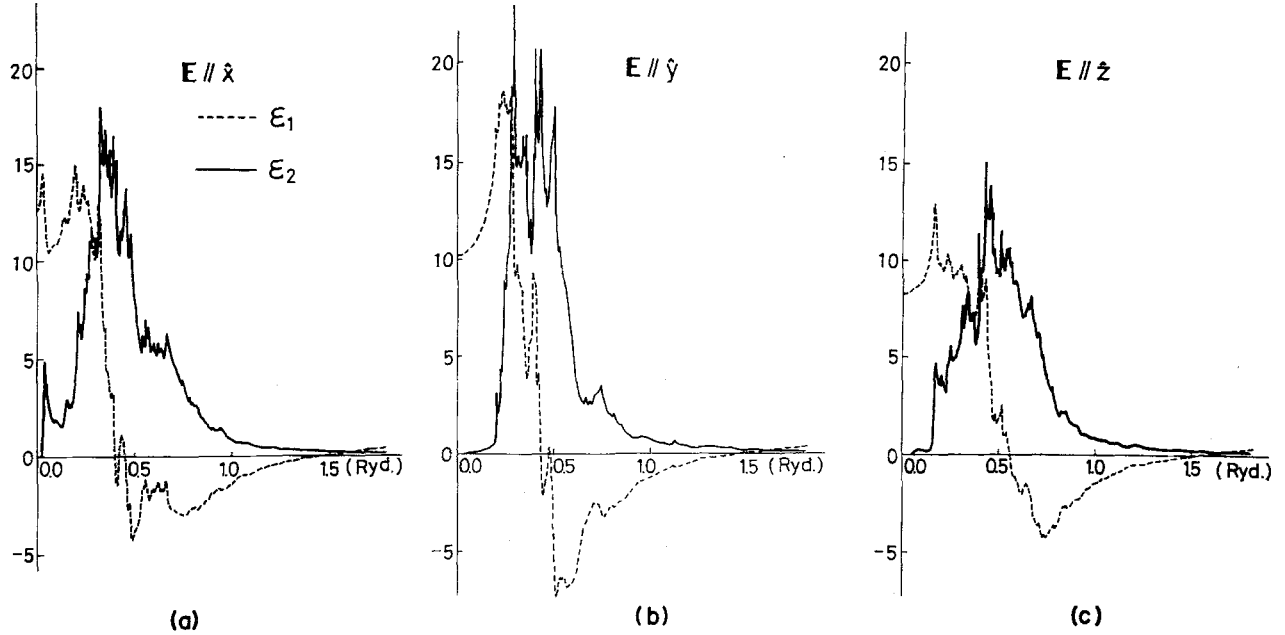


Fig. 7a–c. The calculated frequency-dependent dielectric function [32]; (a) $E \parallel \hat{x}$, (b) $E \parallel \hat{y}$, and (c) $E \parallel \hat{z}$. Broken curves for the real part ϵ_1 and full curves for the imaginary part ϵ_2

van der Waals' gap reduces the gap energy at Z by enlarging the dispersion of the highest valence and lowest conduction bands along the Γ –Z line. On the other hand, the decrease in the bond length d_2 widens the energy gap at Z by enlarging the bonding-antibonding separation associated with the bond d_2 . The self-consistent pseudopotential calculation [21] has disclosed that the observed pressure dependence of the energy gap shown later in Sect. 5.3 (see also Fig. 22) can be explained, if we assume that d_1 and even d_2 remain unchanged, and the bond angle α_2 and the interlayer van der Waals' gap change linearly as the pressure increases up to about 1.2 GPa [17].

DOS of the valence band consists of six peaks, as denoted by ① to ⑥ in Fig. 5. Among them, ① consists of mainly $3p_x$ orbitals, ② of an admixture of $3p$ and $3s$ orbitals, and ③ of $3p_x$ and $3p_y$ orbitals. Peaks ④, ⑤, and ⑥ are essentially made of $3s$ orbitals. A comparison between theory and experiment about DOS will be given in Sect. 4.

The imaginary part of the frequency-dependent dielectric function at zero temperature for linearly polarized light is given by

$$\epsilon_{2\alpha}(\omega) = \frac{4\pi^2 e^2}{m^2 \omega^2} \sum_{i,j}^{B \cdot Z} \sum_k 2|M_{ci,vj}^\alpha(k)|^2 \cdot \delta(E_{ci}(k) - E_{vj}(k) - \hbar\omega), \quad (3)$$

where α denotes the direction of the polarization, c_i and v_j stand for one of the valence and conduction bands, respectively, the sum over wave vector k is performed over the first Brillouin zone, and $M_{ci,vj}^\alpha(k)$ is the

momentum matrix element between the states $\psi_{ci,k}$ and $\psi_{vj,k}$. The real part $\epsilon_{1\alpha}(\omega)$ is calculated from $\epsilon_{2\alpha}(\omega)$ by using the Hilbert transformation. The results are shown in Fig. 7 for the polarizations $E \parallel \hat{x}$, \hat{y} , and \hat{z} [22].

As can be seen from the figure, the imaginary parts equally show a sharp rise at about $\hbar\omega = 0.2$ ryd corresponding to the beginning of the dipole transition from the two-dimensional bonding (valence) $3p$ states to the anti-bonding (conduction) ones.

According to group-theoretical consideration, it can be shown that the dipole transition between the highest valence and the lowest conduction bands is allowed for the polarization $E \parallel \hat{x}$, but forbidden on lines U, Σ , and Γ' for the polarizations $E \parallel \hat{y}$ and \hat{z} . This fact explains that the $\epsilon_{2x}(\omega)$ has a peak starting from the threshold, while $\epsilon_{2y}(\omega)$ and $\epsilon_{2z}(\omega)$ do not.

The zero-frequency limit of the real part of the dielectric function gives the static dielectric constant tensor. Its values are found to be $\epsilon_{xx} = 12.5$, $\epsilon_{yy} = 10.2$, and $\epsilon_{zz} = 8.3$. The corresponding experimental values are obtained from far-infrared interference spectra with thin cleaved samples, being found to be $\epsilon_{xx} = 16.5 \pm 0.1$, $\epsilon_{yy} = 13.0 \pm 0.1$, and $\epsilon_{zz} = 8.3 \pm 0.15$ [23].

The real part for each polarization has a zero at about $\hbar\omega = 1.5$ ryd (≈ 20 eV) which corresponds to the bulk plasmon frequency. Harada et al. [24], Goodman et al. [21a], and Taniguchi et al. [25] measured x-ray photoemission $2p$ and $2s$ core-level spectra of black-P using the Mg K_α line. From the satellite structures of the core levels due to the bulk plasmon excitation, they obtained 20.1, 20.2, and 19.8 eV respectively, as the

bulk plasmon energy, in good agreement with the values determined from the zeros of the real part of the dielectric function.

4. Optical Properties

4.1. Photoelectron Spectroscopy

XPS and UPS data of the valence band of black-P [24, 25] are shown in Fig. 8 together with the theoretical DOS of the valence band. As already shown in Fig. 5, the theoretical DOS of the valence band consists of six peaks, the first three peaks are associated mainly with the $3p$ orbital and the last three ones with the $3s$ orbital. This structure is well reproduced in XPS and UPS spectra. Though correspondence between the calculated DOS and the observed spectra seems excellent, there exists some discrepancy about the energy separation between the peaks ① and ③. Its experimental value is found to be 3.3 eV in [24], 3.1 eV in [21a], and 3.9 eV in [25], while the calculated one is about 4.6 eV.

In Fig. 9 are shown photoelectron spectra of the valence band due to SOR in an energy range around the $2p$ core-exciton excitation energy (120~134 eV) [26]. It can be observed that as the incident photon energy ν becomes larger than the excitation energy of the $2p$ core-exciton (130 eV), the intensity of a peak at 10.8 eV increases and furthermore a new peak emerges on the left-hand side of it, shifting toward the high energy with increasing ν . This new peak can be attributed to $L_{2,3}$ VV Auger structure.

In Fig. 10, the photoemission intensities of peaks at 2.7 and 10.8 eV are shown as a function of the incident photon energy [26]. As is seen from the figure, the intensity of the 2.7 eV peak shows a weak Fano-type antiresonance and that of the 10.8 eV peak displays a rapid increase around $\nu=130$ eV and thereafter decreases rather slowly. According to Kotani and Nakano [27], one can attribute the Fano-type modu-

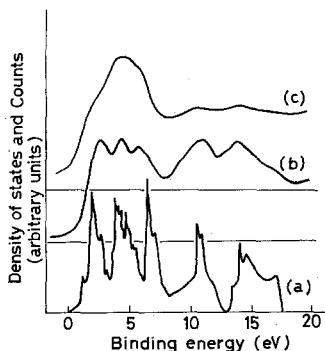


Fig. 8a-c. Comparison of the calculated density of states (DOS) with XPS and UPS spectra (a) DOS of the valence band [21], (b) XPS [24], and (c) UPS [25]

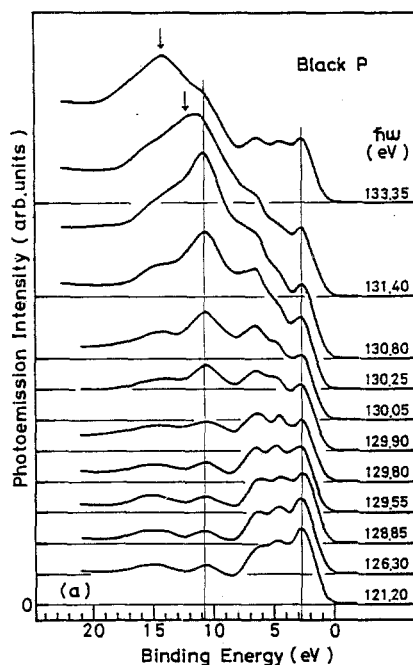


Fig. 9. Angle-integrated photoemission spectra of black-P for excitation photon energy between 120 and 134 eV. The arrows indicate the $L_{2,3}$ VV Auger structure [26]

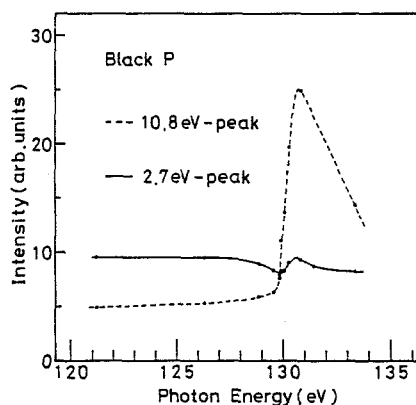


Fig. 10. Plots of 10.8 eV- and 2.7 eV-peaks' intensities in Fig. 9 as a function of excitation photon energy [26]. That of 10.8 eV-peak is shown by dashed curve and that of 2.7 eV-peak by a solid curve

ation of the 2.7 eV peak to the interference between the direct $3p$ band photoemission and the resonant enhancement of the 10.8 eV peak due to the excitation of the core exciton followed by the LVV Auger process. Angle-resolved ultraviolet photoemission spectroscopy (ARUPS) is a very useful experimental means to get direct information concerning the energy-band dispersion of crystals, especially of layered crystals such as black-P. Figure 11 shows the energy band along the $\Gamma-X$ and $Z-\Gamma$ lines calculated by Asahina et al. [21] and those determined by Takahashi et al.

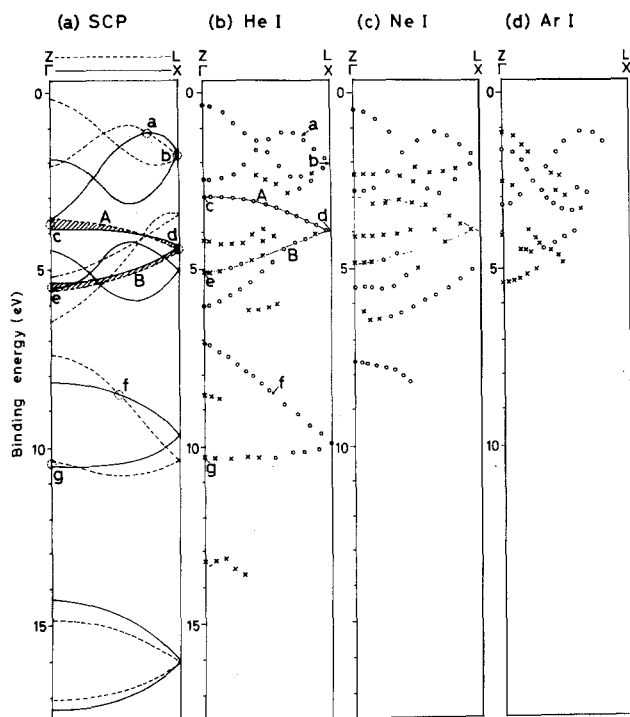


Fig. 11a-d. Calculated and experimental bands of black-P in the Γ -X-L-Z plane [30]. (a) the self-consistent pseudopotential (SCP) calculation along the Γ -X (full curve) and Z-L (broken curve) lines. (b)-(d) experimental bands derived from the He I, Ne I, and Ar I measurements [21]. For the meaning of small and capital letters see the text

[29-31] using ARUPS. Figure 12 illustrates similar results along the T and T' lines.

The overall features of the calculated band structure are well reproduced in the experimental data, though there are some slight discrepancies between them. Here

it should be noted that the experimental data were determined by neglecting the energy dispersion along the layer-stacking z direction. In order to avoid the ambiguity due to this neglect in comparing the experimental and calculated results, they picked out some special points and bands in the calculation, which have practically no interlayer dispersion. These points and bands are indicated in the figures by small (a-n) and capital (A-E) letters, respectively. These are relatively easily distinguishable in ARUPS spectra because the electronic states with no interlayer dispersion should form a sharp and rather strong peak in photoemission spectra.

Bands A and B, and points c, d, and e are located at about 0.5 eV larger binding energies in the calculation than the experiment. On the other hand, the calculated points a and b are shifted slightly by about 0.2 eV toward a smaller binding energy, compared with the experiment. These facts mean that the calculation overestimates the $3p$ band width by about 0.7 eV. This is consistent with the observation in comparing calculated DOS with the XPS spectra mentioned before.

4.2. Optical Properties due to Electronic Excitation

Absorption spectra of a cleaved thin film of black-P for linearly polarized light near the absorption threshold are shown in Fig. 13 [32]. The results indicate that in accordance with the band calculation [21] the transition at the absorption threshold is allowed for the polarization $E \parallel \hat{x}$ and is forbidden for the polarization $E \parallel \hat{y}$.

Figure 14 shows the reflectance spectrum observed at liquid He temperature, and its Kramers-Kronig-

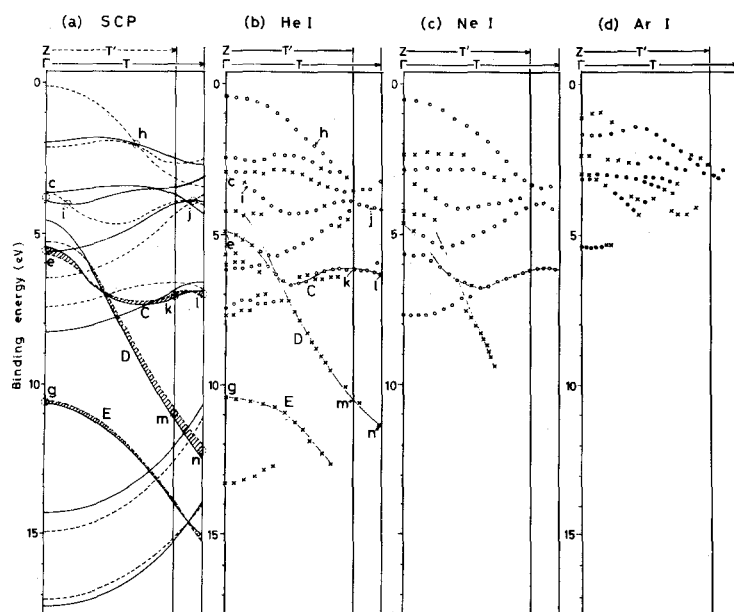


Fig. 12a-d. Calculated and experimental bands of black-P [30]. (a) Calculated bands along the Γ -T (full curve) and Z-T' (broken curve) directions. (b) and (c) experimental bands determined from the He I and Ne I measurements, respectively [29]. For the meaning of small and capital letters see the text

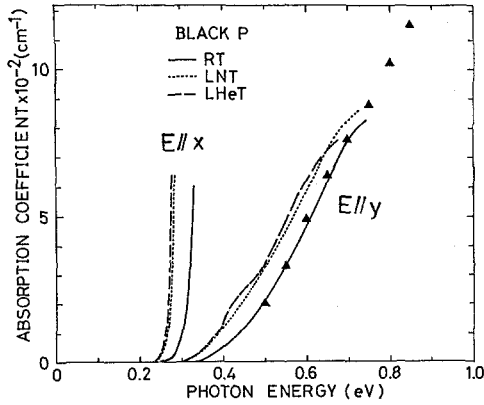


Fig. 13. Absorption spectra near the threshold of black-P for linearly polarized light incident on the cleaved xy plane with the polarization $E//x$ and $E//y$ at various temperatures [32]. Solid lines at room temperature, dotted lines at liquid N_2 temperature, and broken lines at liquid He temperature

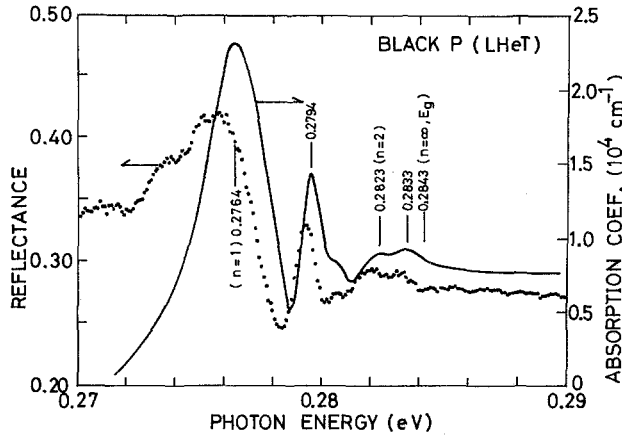


Fig. 14. Reflection spectrum (dots) of black-P at liquid He temperature for linearly polarized light with the polarization $E//x$ and absorption spectrum (solid line) obtained by a Kramers-Kronig transformation [32]

transformed absorption coefficient spectrum (solid curve) for linearly polarized light with the polarization $E//x$ [32]. In the figure, the excitonic structure of the direct allowed type is observed clearly. An absorption peak at 0.2794 eV was considered extrinsic, since it was rather sensitive to experimental conditions such as the time between cleavage and measurement, the degrees of vacuum and temperature, and the lack of reproducibility.

Assuming the hydrogen-like model for the exciton and assigning peaks at 0.2764 and 0.2823 eV to transitions to the $n=1$ and $n=2$ levels, respectively, one can obtain 0.2843 eV for the $n=\infty$ level and 7.9 meV for the binding energy of the exciton E_b . If one assumes tentatively the average dielectric constant $\epsilon=12$ according to the observed static dielectric tensor [23] (see

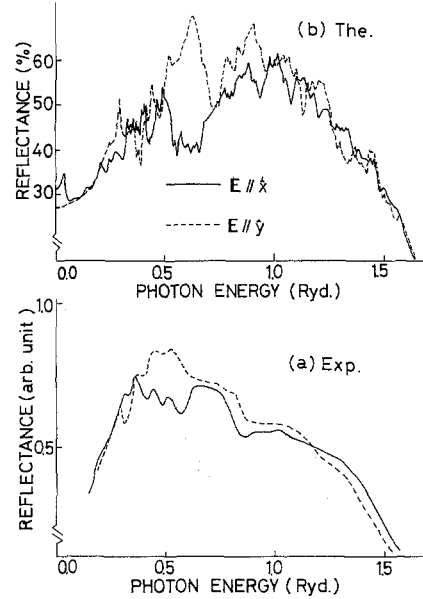


Fig. 15a and b. Reflection spectra on the cleaved xy plane in the region from visible to vacuum ultraviolet: (a) experimental curves by Taniguchi et al. [33] and (b) calculated curves [22]. Solid lines are for the polarization $E//x$ and broken ones for the polarization $E//y$

also Sect. 3), the effective exciton mass is estimated to be $0.084 m_0$ (m_0 : true electron mass), which is a reasonable value compared with the cyclotron masses of electrons and holes shown later in Sect. 5.1.

The reflectance spectra of black-P in the region from the visible to the vacuum ultraviolet (3~20 eV) were obtained by Taniguchi et al. using linearly polarized SOR incident on a cleaved surface [33]. Their results are shown in Fig. 15 together with corresponding theoretical results calculated from the frequency-dependent dielectric function in the previous section. The overall features of the experimental spectra including the prominent polarization dependence around $\hbar\omega=0.5$ ryd are well reproduced in the calculated ones, except that the polarization-sensitive region in the calculation is shifted by about 1.5 eV toward a higher energy compared with the experiment.

Hayashi et al. [34] obtained soft x-ray emission (K_β emission) and absorption (K absorption) spectra of a black-P single crystal polarized along the crystalline x , y , and z axes, as shown in Fig. 16. Such spectra give us direct information about the partial density of states originating from each of the $3p$ atomic orbitals.

The experimental results indicate that at first the upper part of the valence band near the Fermi level is largely contributed by the $3p_z$ states in accordance with the band calculation (Sect. 3), secondly the $3p_y$ states form the middle to the lower part of the $3p$ valence band, thirdly the $3p_x$ states spread over a whole range in the band, and lastly the absorption spectra (corresponding

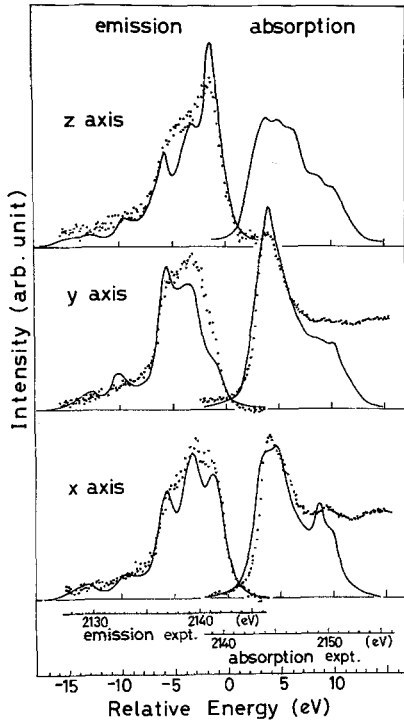


Fig. 16. K_{β} emission and K absorption spectra of black-P [34]. The energy zero for experimental emission spectra (dots) is so adjusted that the position of the highest peak in the $K_{\beta z}$ emission is aligned with that which is calculated (solid line). As for the absorption spectra, the peak position of the K_y spectrum is aligned. The energy on the abscissa for the calculated curves is a value relative to the Fermi level in the band calculation

to the conduction band) also show clear dependence on the polarization.

The theoretical K_{β} emission and K absorption spectra shown by solid curves in Fig. 16 were calculated to be compared with the experimental results. The calculated results were obtained by convolution, with a Lorentzian curve of 1.0 eV width, of the theoretical spectra calculated from the results of the band calculation based on the self-consistent pseudopotential method [21]. It should be noted here that the experimental absorption spectra are shifted by about 2 eV toward a higher energy compared with the experimental emission data to get a better correspondence between the experiment and the calculation. Agreement between experiment and calculation is excellent except for the intensity of K_{β} emission spectrum at about 2137.5 and 2139.5 eV. This disagreement in K_{β} emission corresponds to the inconsistency between the theoretical and experimental band structure observed in ARUPS (Sect. 4.1).

The most serious discrepancy between experiment and calculation lies in a relative displacement between the emission and absorption spectra. As mentioned above, to get good agreement, we have to shift the experi-

mental absorption spectra as a whole toward a higher energy by about 2 eV. This is consistent with the discrepancy between calculation and experiment observed in the reflectance spectra in the region from the visible to the vacuum ultraviolet (Fig. 15).

4.3. Optical Properties due to Phonon Excitation

Since it contains four atoms in a primitive cell, black-P has twelve phonon branches. Dispersion curves of these phonon branches were calculated by Kaneta et al. using the least-square-fitting method based on the valence-force field model (VFFM) [35] and the bond charge model (BCM) [36]. Figure 17 shows the results calculated by BCM. The whole branches are separated into two groups with a frequency gap between them, each of which contains six branches. The high-frequency group is of the bond-stretching type and the low-frequency one of the bond-bending type in character. The consequences of the layer structure appear in some features of the phonon dispersion curves. First of all, in the [001] direction, the optical branches are almost dispersionless and the sound velocities are smaller than those in other directions. Secondly, the phonon dispersion curves along the line $\Gamma-T-T'-\Sigma$ are nearly symmetric as a whole about the middle point of the line. Thirdly TA_z (TA mode polarized in the z direction) in the [100] and [010] directions have concave dispersion for small k near the point Γ .

Optical Γ phonons in black-P consist of six Raman active, two infrared active and one inactive modes. The first-order Raman spectra in black-P have been measured by several groups [37–39]. Comparison between experiment and calculation by BCM are shown in Table 2 with excellent agreement.

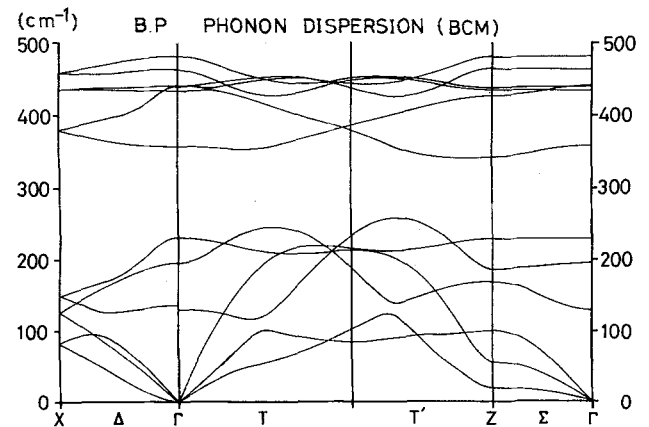


Fig. 17. Phonon dispersion curves of black-P calculated using the bond charge model (BCM) [36]. A discontinuity observed at Γ corresponds to the Lyddane-Sacks-Teller splitting of the infrared active optical Γ_3^- phonon. That of the infrared active optical Γ_4^- phonon is too small to be shown

Table 2. Energies of optical Γ phonon in black-P in cm^{-1}

Symmetry	Type	Observed		Calculation
		Lannin and Shanabrook [37]	Sugai and Shirotani [39] in parentheses [38]	Kaneta and Morita [36]
$\Gamma_1^+(A_g)$	Raman	471	470 (467)	480
$\Gamma_1^+(A_g)$	Raman	365	365 (362)	356
$\Gamma_2^+(B_{2g})$	Raman	436	442	439
$\Gamma_2^+(B_{2g})$	Raman	230	233	228
$\Gamma_3^+(B_{1g})$	Raman	195	197 (194)	194
$\Gamma_4^+(B_{3g})$	Raman	441	440 (439)	439
$\Gamma_4^-(B_{3u})$	Infrared	(TO)471	(TO)468 (LO)470	(TO)461 (TO)462
$\Gamma_3^-(B_{1u})$	Infrared	<200	(TO)136 (LO)138	(TO)129 (LO)135

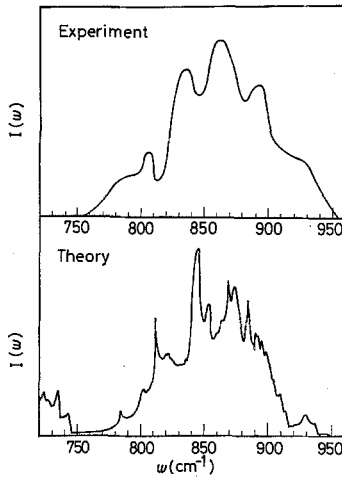


Fig. 18. Second-order Raman spectrum by Lannin and Shanabrook (above) [37] and calculated two-phonon frequency distribution function (below) [35]

The second-order Raman spectra due to two-phonon processes were measured by Lannin and Shanabrook [37]. Figure 18 shows the observed spectrum and the two-phonon frequency distribution function between 750 and 950 cm^{-1} which has been calculated from the phonon dispersion by VFFM [35]. Correspondence between experiment and calculation seems very good. Note that the calculation does not take account of the transition matrix element, however.

Black-P is interesting to the extent that it has two infrared active Γ phonons in spite of its homopolar character. The first preliminary measurement of the infrared absorption due to the one-phonon process in black-P was performed by Lannin and Shanabrook [37]. After that, Ikezawa et al. [40], Terada et al. [41], and Sugai and Shirotani [42] determined frequencies and types of polarization of these two phonons.

Especially Sugai et al. succeeded in observing the Lyddane-Sacks-Teller splitting of these phonons, which is probably the first observations in such a homopolar covalent crystal as black-P.

As already mentioned, the lattice dynamics of black-P was calculated by VFFM and BCM. The frequency of the infrared active phonon, Γ_3^- , calculated by VFFM is 213 cm^{-1} in contrast with its observed value of about 130 cm^{-1} . The origin of this discrepancy is attributed to the fact that VFFM does not contain freedom describing polarization associated with infrared active modes. On the other hand, BCM is free from such a shortcoming and its results can explain observed frequencies and the Lyddane-Sacks-Teller splitting of these modes, as shown in Table 2.

Ikezawa et al. [40] measured infrared absorption spectra due to two-phonon excitation using incident light linearly polarized parallel to the cleaved surface and found remarkable polarization dependence. In Fig. 19a are shown the observed absorption spectra and in Fig. 19b the corresponding two-phonon density of states. The counterpart of each peak in the observed spectra can be found generally in the two-phonon density of states, as indicated by a small and the corresponding capital letter in the figure. In order to explain, theoretically and quantitatively, the polarization dependent spectra, however, one has to take account of the effect of the transition matrix element for two-phonon processes. Such a task is left to a future study.

5. Semiconducting Properties

5.1. Cyclotron Resonance

As mentioned before in Sect. 3 (see also Table 3), the results of the band calculation of black-P [20, 21]

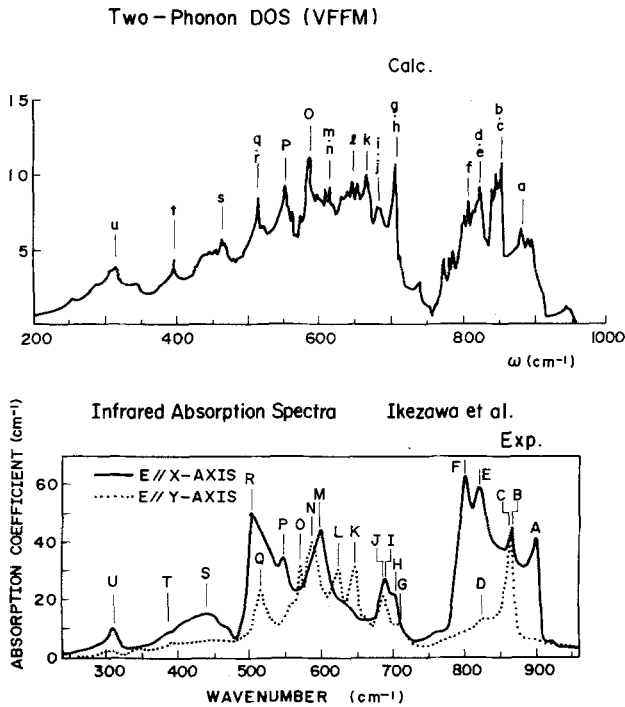


Fig. 19. (a) Two-phonon frequency distribution function [35] and (b) infrared absorption spectra due to two-phonon excitation for linearly polarized light incident on the cleaved xy plane [40]. For the meaning of small and capital letters see the text

Table 3. Effective masses of carriers in black-P

Direction	Hole		Electron	
	Expt. [43]	Calc. [21]	Expt. [43]	Calc. [21]
m_x/m_0	0.076	0.09	0.0826	0.09
m_y/m_0	0.648	0.81	1.027	1.16
m_z/m_0	0.280	0.36	0.128	0.17

indicate that for both the electron and the hole the effective mass anisotropy in the xy plane is fairly large, that the effective mass in the x direction is lightest, and that that in the layer-stacking z direction is lighter than that in the in-plane y direction in spite of the layered structure.

These interesting predictions have been confirmed by measurement of far-infrared cyclotron resonance absorption in p- and n-type samples [43]. The observed effective masses are listed in Table 3 together with the calculated ones. The theoretical values obtained by the self-consistent pseudopotential method (SCPM) are in better agreement with the observed ones than those of the tight binding method. It is interesting to see that the average effective mass defined by $(m_x m_y m_z)^{1/3}$ is $0.22 m_0$ for an electron and $0.24 m_0$ for a hole and these values are one order of magnitude larger than the electron

mass of $0.024 m_0$ in InAs which has an energy gap of 0.36 eV similar to black-P.

5.2. Electrical Conduction and Carrier Mobilities

Measurements of the electrical conductivity and the Hall effect were performed already in 1953 by Keyes [2] and in 1963 by Warschauer [3] using polycrystalline samples. They disclosed that all samples measured were p-type narrow-gap semiconductors with gap energies of about 0.3 eV. Since then, further measurement has not been made until recently. In 1983 Narita's group made a detailed study of this problem using p- and n-type single crystal samples in the wide temperature range from 4.2 to 550 K [44].

Undoped samples are always of p-type and show a positive Hall coefficient in the whole temperature range under investigation. The results imply that the hole carrier is more conductive than the electron one. The carrier density calculated from the Hall coefficient indicates that the intrinsic temperature range starts from about 220 K. The energy gap determined from the temperature dependence of the conductivity in the intrinsic region is 335 meV, while the one determined optically at liquid He temperature is 284.3 meV (Sect. 4.2).

The effective concentration of acceptors in p-type samples ($N_A - N_D$) is $2 \sim 5 \times 10^{15} \text{ cm}^{-3}$. Samples doped with Te atoms contain donors of the effective concentration ($N_D - N_A$) of $2 \sim 3 \times 10^{16} \text{ cm}^{-3}$ and show the inversion from p-type to n-type conduction at about 220 K, becoming n-type in the low-temperature region. The ionization energy of an impurity level determined from the temperature dependence of the conductivity in the low-temperature region is 18 meV for acceptors in p-type samples and 20 meV for donors in n-type samples [45].

The origin of donors in Te-doped n-type samples can be attributed to Te atoms of hexavalency substituted for P atoms of pentavalency. On the other hand, that of acceptors in p-type samples is not yet clear.

Hall mobilities of hole and electron in black-P are shown in Fig. 20a and b as a function of temperature [44]. One of the remarkable things observed from the figure is, first of all, that the anisotropy in mobilities is significantly different from an expectation of its carrier effective masses. Namely, the smallest mobilities are in the layer-stacking z direction, while the heaviest effective masses are in the in-plane y direction. The other is that the temperature dependence of the Hall mobilities obeys, in the temperature range between 50 and 200 K, the $T^{-3/2}$ law characteristic of the acoustic phonon scattering.

Morita et al. [47] analysed the anisotropic mobilities of black-P using the deformation potential model and

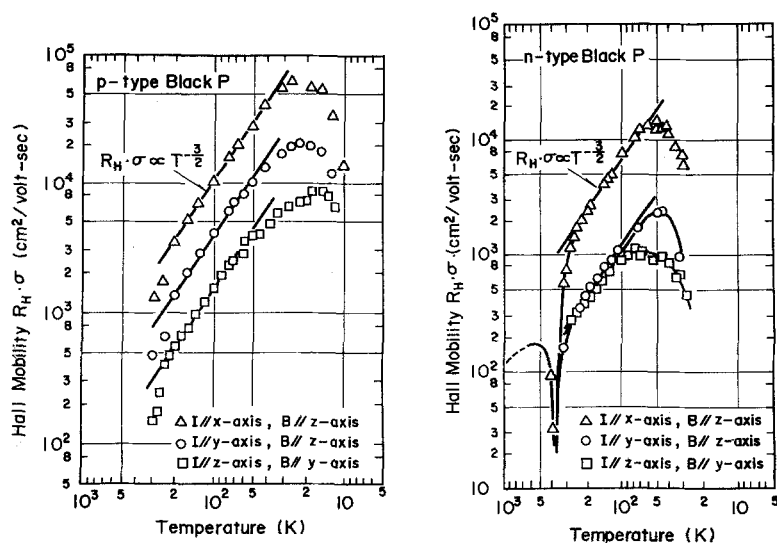


Fig. 20a and b. Logarithmic Hall mobility vs. logarithmic temperature curves for (a) p-type and (b) n-type samples of black-P [44]

Table 4. Electrical properties of black-P [44]

Direction	Hole			Electron		
	x	y	z	x	y	z
Hall mobility (cm ² /V·s) at 200 K	3000	1200	540	2300	460	400
Max. value $\times 10^{-3}$	65	20	8.5	16	2.2	1.0
Activation energy of impurity [meV]	~ 18			~ 20		
Effective impurity concentration [cm ⁻³]	$2 \sim 5 \times 10^{15}$			$2 \sim 3 \times 10^{16}$		
Energy gap E_g at room temp. [meV]	335					

the results of the lattice dynamics calculated in terms of VFFM [35] (see also Sect. 4.3). As a result, it is shown that to explain the experimental results about the anisotropic mobilities one has to assume a highly anisotropic deformation potential tensor which may be expected from the special feature of the band structure.

The electronic properties of black-P discussed above are summarized in Table 4.

5.3. Pressure Effect on the Band Structure

Bridgeman [48] and Keyes [2] measured the electrical resistivity of black-P under a pressure up to 2 and 0.8 GPa, respectively. Recently Narita's group made detailed investigations on this problem using single-crystal samples [49, 50].

In Fig. 21, the resistivities at room temperature along the principal crystal axes $x(c)$, $y(a)$, and $z(b)$ measured by Akahama et al. [50] are shown as a function of pressure up to 5.5 GPa. The resistivities decrease logarithmically as the pressure increases and show two anomalies at about 1.7 and 4.2 GPa. Whereas the anomaly at 4.2 GPa is attributed to the transition from the orthorhombic to the rhombohedral structure, any structural change has not been reported around 1.7 GPa. As will be shown just below, the energy gap decreases with increasing pressure, becoming zero around 1.7 GPa. Namely, the type of conduction changes from semiconducting to metallic without any phase change.

The temperature dependence of the resistivity shown in Fig. 22 [50] indicates that at a pressure lower than

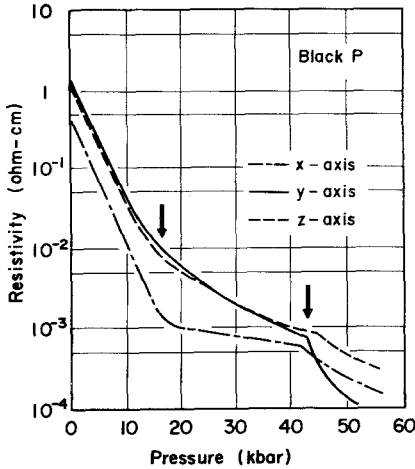


Fig. 21. Resistivity vs. pressure relation of black-P along the x, y, and z directions at 300 K [50]

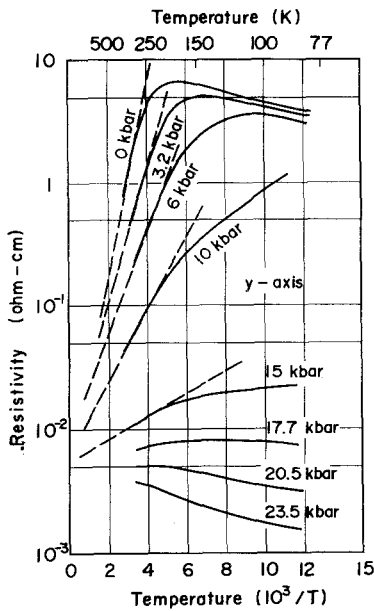


Fig. 22. Logarithmic resistivity vs. reciprocal temperature along the y direction of black-P at various pressures [50]

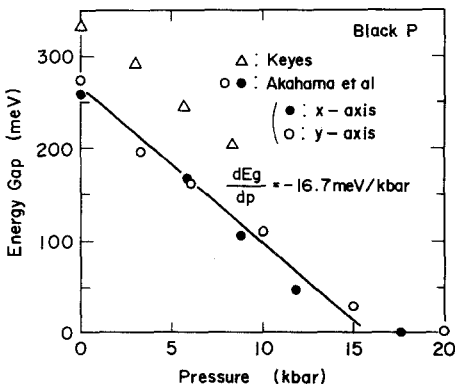


Fig. 23. Pressure dependence of the energy gap E_g which is determined from the slopes of the broken lines in Fig. 22 [50]. The results obtained by Keyes [2] are shown, too

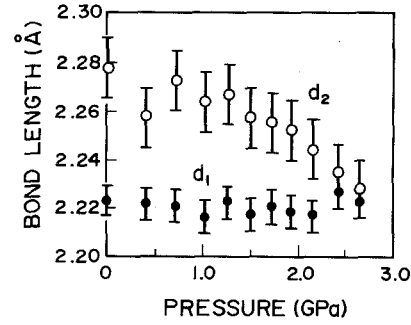


Fig. 24. Bond lengths in black-P vs. pressure: solid circles: d_1 and empty ones: d_2 [15]

1.7 GPa the conduction is semiconducting, but at a pressure higher than that it is metallic. The energy gap vs. pressure relation determined from the resistivity in the intrinsic region is shown in Fig. 23 together with the results by Keyes [2]. The pressure coefficient of the energy gap, dE_g/dP , estimated from the data is found to be -167 meV/GPa . This magnitude is large compared with those of other semiconductors.

According to discussions in Sect. 2, a decrease of the bond length d_2 gives rise to an increase of the energy gap and that of the van der Waals gap between successive two layers to a decrease of the energy gap. The hydrostatic pressure dependence of the bond lengths d_1 and d_2 measured by Cartz et al. [15] is shown in Fig. 24. As seen from the figure, the bond length d_1 remains almost unchanged as pressure increases, but the bond length d_2 shows a somewhat complicated behavior. Two different ways of understanding the pressure dependence of d_2 seem possible within the accuracy of the data: A) one of them is that d_2 decreases linearly as the pressure increases up to about 3 GPa, where it becomes equal to d_1 . B) The other is that d_2 remains nearly unchanged up to about 1.7 GPa and then decreases linearly as the pressure increases beyond it, becoming equal to d_1 at about 3 GPa.

Asahina et al. performed the calculation of dE_g/dP based on the self-consistent pseudopotential method [21] using the observed linear compressibilities [15] (see also Sect. 2.2) and B) mentioned above, and obtained -235 meV/GPa . Later, Sasaki et al. revised their calculation and obtained -212 meV/GPa [17]. They also showed that the adoption of A) mentioned above gives us -74 meV/GPa instead. These results indicate that the reality is somewhere near B) between A) and B).

As mentioned above, black-P decreases its energy gap linearly with increasing pressure and reveals a semiconductor-metal transition due to overlap between conduction and valence bands without any

structural change at about 1.7 GPa. The actual structural change from the orthorhombic to the rhombohedral structure takes place at the much higher pressure of about 5 GPa. Thus Akahama et al. suggested that the so-called excitonic phase might be observed in black-P [50].

6. Superconductivity in Black-P under High Pressure

As already explained in Sect. 2, black-P shows an interesting sequence of structural transformations under pressure from the semiconducting orthorhombic phase to the semimetallic rhombohedral phase at about 5 GPa, to the metallic simple cubic phase at about 10 GPa.

In 1968, Berman and Brandt [51] and Wittig and Mathias [52] observed the superconductivity with $T_c = 6$ K in the metallic simple cubic phase. Recently, Kawamura et al. [7] noted interesting pressure-induced superconductivity in a single crystal of black-P.

In order to investigate the dependence of the superconductivity of black-P on treatment such as cooling and pressurizing they performed measurement along the following three paths [53, 54].

Path (A): After applying a pressure of up to 15 GPa at room temperature so that the samples are transformed into the simple cubic phase completely, the pressure cell is cooled down to liquid He temperature and then the pressure dependence of the superconducting transition temperature T_c is measured.

Path (B): After applying a pressure of up to 8.7 GPa at room temperature so that the samples are transformed into the rhombohedral phase completely, the pressure cell is cooled down to liquid He temperature and then the pressure dependence of T_c is measured like the case path (A).

Path (C): Samples are first cooled down to liquid He temperature at normal pressure and then the pressure dependence of T_c is measured by applying a high pressure.

These three paths are shown schematically together with the phase diagram of black-P in Fig. 25.

The pressure dependence of T_c in each path is illustrated in Fig. 26. It was observed that residual resistivities, just before the transition, were of the order of $10^{-5} \Omega\text{cm}$ and the remnant resistivities below the termination point of the transition were of order of $10^{-7} \Omega\text{cm}$. The remnant resistivities are attributed to the contact resistance and the resistivity of the sample itself is considered to be nearly zero.

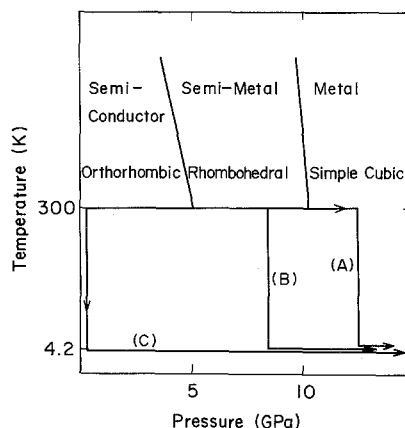


Fig. 25. Schematic phase diagram of black-P. Three different paths, (A), (B), and (C), along which measurement on the pressure dependence of the superconducting transition temperature was done, are also illustrated

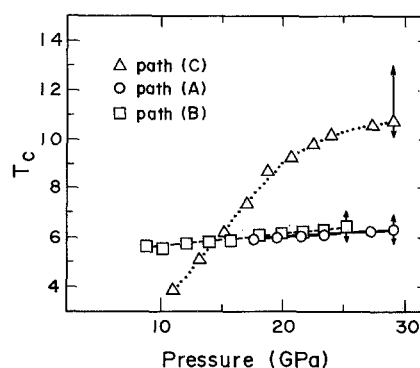


Fig. 26. Pressure dependence of T_c . T_c along path (A) is indicated by circles, along path (B) by squares and along path (C) by triangles [7]

In path (A), T_c is about 6 K as in [51, 52] and increases slightly with increasing pressure. It is also remarkable that T_c remains around 6 K for several hours even after removing the applied pressure at liquid He temperature.

In path (B), a broad transition is observed at 8.7 GPa, suggesting the possibility of superconductivity in the rhombohedral phase. The transition becomes sharper, gradually with increasing pressure, and the transition curve at about 25 GPa resembles those in path (A). This fact suggests that the transformation from the rhombohedral to the simple cubic structure may take place even at liquid He temperature.

In path (C), T_c starts from 4 K at 11 GPa, increases with increasing pressure and becomes 10.7 K at about 30 GPa, where the width of the transition is $2 \sim 3$ K, and the starting temperature of the transition is 13 K. This transition temperature is the highest one observed in non-transition elements so far. It is also to be noted that the transition temperature decreases rapidly by

decreasing the applied pressure and becomes null before about 3 GPa in contrast with the case of path (A).

For the mechanism of the superconductivity in path (C), Kawamura et al. proposed a model [7]. Accordingly, there are many dislocations in these compressed samples. Atoms surrounding dislocations may be relatively so mobile that the transition from the orthorhombic to the simple cubic phase via the rhombohedral phase will take place around dislocations even at low temperature. Thus, black-P is probably converted in a mixed system consisting of metallic fine threads dispersed in the semiconducting matrix. They considered that the appearance of superconductivity in a system like this might be possible according to the mechanism suggested by Fukuyama [55].

Another mechanism of the superconductivity is possible, however. As seen in Sect. 5.3, the energy gap in the semiconducting orthorhombic phase decreases rather rapidly with increasing pressure and becomes zero at about 1.7 GPa, showing the semiconductor-metal transition accompanied by no structural change. Therefore, the superconductivity observed in the case of path (C) may be considered as the special property of black-P under high pressure, clamped in the orthorhombic structure by cooling it down to liquid He temperature.

7. Summary

In this review of recent research work on black-P, which is a narrow-gap semiconductor newly attracting attention because of recent success in growing large single crystals, I covered the preparation, the crystal structure, the band structure, the optical and electrical properties, and the superconductivity. On account of limited space, however, I could not touch on the following problems: alloying with As, the intercalation compounds, theoretical and experimental details of the lattice dynamics, the mechanism of the pressure-induced phase transformations, the electronic structure of the high-pressure phases, in connection with these topics, comparisons with As and Sb, and so on. In conclusion, research on black-P has just started and is offering a rapidly developing new and interesting field. Very likely, some surprises in this field may be forthcoming.

Acknowledgements. The author wishes to thank the members of his research group for their valuable collaboration and suggestions in the course of this work. His thanks are also due to numerous colleagues who made their work available to him in print form. He wishes to especially thank Dr. H. Asahina, T. Takahashi, M. Taniguchi, and S. Sugai, Prof. T. Sagawa, Y.

Kondo, M. Ikezawa, and S. Endo. He also acknowledges the financial support from the Special Project Research on the Properties of Molecular Assemblies (No. 59112004) from the Ministry of Education, Science, and Culture.

References

1. J. Donohue: *The Structures of the Elements* (Wiley, New York 1974)
2. R.W. Keyes: *Phys. Rev.* **92**, 588 (1953)
3. D. Warschauer: *J. Appl. Phys.* **34**, 1853 (1963)
4. Y. Maruyama, S. Suzuki, K. Kobayashi, S. Tanuma: *Physica* **47**, 99 (1981)
5. P.W. Bridgeman: *J. Am. Chem. Soc.* **36**, 1344 (1914); **38**, 609 (1916); *Proc. Am. Acad. Art Sci.* **62**, 207 (1927); **76**, 55 (1948); **70**, 71 (1935)
6. J.C. Jamieson: *Science* **139**, 1291 (1963)
7. H. Kawamura, I. Shirotni, K. Tachikawa: *Solid State Commun.* **49**, 899 (1984)
8. D. Schiferl: *Phys. Rev. B* **19**, 806 (1979)
9. H. Asahina, K. Shindo, A. Morita: *J. Phys. Soc. Jpn. Suppl.* **49**, 85 (1980)
10. I. Shirotni, R. Maniwa, H. Sato, A. Fukizawa, N. Sato, Y. Maruyama, T. Kajiura, H. Inokuchi, S. Akimoto: *Nippon Kagaku Kaishi* (1981) No. 10, 1604 (in Japanese)
11. S. Endo, Y. Akahama, S. Terada, S. Narita: *Jpn. J. Appl. Phys.* **21**, L482 (1982)
12. A. Brown, S. Rundqvist: *Acta Cryst.* **19**, 684 (1965)
13. Y. Akahama, S. Endo, S. Narita: *J. Phys. Soc. Jpn.* **52**, 2148 (1983)
14. J.C. Slater, G.F. Koster, J.H. Wood: *Phys. Rev.* **126**, 1307 (1962)
15. L. Cartz, S.R. Srinivasa, R.J. Riedner, T.D. Jorgensen, T.G. Worlton: *J. Chem. Phys.* **71**, 1718 (1979)
16. T. Kikegawa, H. Iwasaki: *Acta Cryst. B* **39**, 158 (1983)
17. T. Sasaki, A. Morita: To be published
18. H. Iwasaki, T. Kikegawa, T. Fujimura, S. Endo, Y. Akahama, T. Akai, O. Shimomura, S. Yamaoka, T. Yagi, S. Akimoto, I. Shirotni: *Proc. Xth AIRAPT High Pressure Conf. 1985* (Amsterdam) (to be published)
19. I. Shirotni, A. Fukizawa, H. Kawamura, T. Yagi, S. Akimoto: In *Solid State Physics under Pressure*, ed. by S. Minomura (KTK, Tokyo 1985) p. 207
20. Y. Takao, H. Asahina, A. Morita: *J. Phys. Soc. Jpn.* **50**, 3362 (1981)
21. H. Asahina, K. Shindo, A. Morita: *J. Phys. Soc. Jpn.* **51**, 1192 (1982)
- 21a. N.B. Goodman, L. Ley, D.W. Bullett: *Phys. Rev. B* **27**, 7440 (1983)
22. H. Asahina, A. Morita: *J. Phys. C* **17**, 1839 (1984)
23. T. Nagahama, M. Kobayashi, Y. Akahama, S. Endo, S. Narita: *J. Phys. Soc. Jpn.* **54**, 2096 (1985)
24. Y. Harada, K. Murano, T. Takahashi, Y. Maruyama: *Solid State Commun.* **44**, 877 (1982)
25. M. Taniguchi, S. Suga, M. Seki, K. Sakamoto, H. Kanzaki, Y. Akahama, S. Endo, S. Narita: *Solid State Commun.* **45**, 59 (1983)
26. M. Taniguchi, S. Suga, M. Seki, H. Sakamoto, H. Kanzaki, Y. Akahama, S. Endo, S. Terada, S. Narita: *Solid State Commun.* **49**, 867 (1984)
27. A. Kotani, T. Nakano: *Solid State Commun.* **51**, 97 (1984)
28. T. Takahashi, K. Shirotni, S. Suzuki, T. Sagawa: *Solid State Commun.* **45**, 945 (1983)

29. T. Takahashi, H. Tokailin, S. Suzuki, T. Sagawa, I. Shirotani: Phys. Rev. B **29**, 1105 (1984)
30. T. Takahashi, H. Tokailin, S. Suzuki, T. Sagawa, I. Shirotani: J. Phys. C **18**, 825 (1985)
31. T. Takahashi, Y. Hayashi, H. Tokailin, H. Asahina, A. Morita, T. Sagawa, I. Shirotani: Proc. 17th Intern. Conf. Phys. on Semicond. San Francisco (Springer, New York 1984)
32. Y. Kondo, M. Ikezawa: Physics Monthly (in Japanese) **6**, 395 (1985)
33. M. Taniguchi, S. Suga, S. Shin, H. Sakamoto, H. Kanzaki, Y. Akahama, S. Endo, S. Narita: Activity Rep. Synchrotron Radiation Lab. ISSP (1982) p. 17
34. Y. Hayashi, T. Takahashi, H. Asahina, T. Sagawa, A. Morita, I. Shirotani: Phys. Rev. B **30**, 1891 (1984)
35. C. Kaneta, H. Katayama-Yoshida, A. Morita: Solid State Commun. **44**, 613 (1982)
36. C. Kaneta: A thesis submitted to Tohoku Univ. in partial fulfilment of requirements for a degree of Dr. Sc. (1985) (unpublished) and A. Morita: Physics Monthly (in Japanese) **6**, 372 (1985)
37. J.S. Lannin, B.V. Shanabrook: *Physics of Semiconductors*, ed. by B. L. Wilson, Inst. Phys. Conf. Ser. **43**, 643 (London 1978)
38. S. Sugai, T. Ueda, K. Murase: J. Phys. Soc. Jpn. **50**, 3356 (1981)
39. S. Sugai, I. Shirotani: Solid State Commun. **53**, 753 (1985)
40. M. Ikezawa, Y. Kondo, I. Shirotani: J. Phys. Soc. Jpn. **52**, 1518 (1983)
41. S. Terada, T. Hattori, M. Kobayashi, Y. Akahama, S. Endo, S. Narita: J. Phys. Soc. Jpn. **52**, 2630 (1983)
42. S. Sugai, I. Shirotani: Solid State Commun. **53**, 753 (1985)
43. S. Narita, S. Terada, S. Mori, K. Muro, Y. Akahama, S. Endo: J. Phys. Soc. Jpn. **52**, 3544 (1983)
44. Y. Akahama, S. Endo, S. Narita: J. Phys. Soc. Jpn. **52**, 2148 (1983)
45. The ionization energy of donor was originary reported as 39 meV in [44] and was then corrected as 20 meV by taking account of the compensation effect in [46].
46. Y. Akahama, S. Endo, S. Narita: Physics Monthly (in Japanese) **6**, 386 (1985)
47. A. Morita, H. Asahina, C. Kaneta, T. Sasaki: Proc. 17th Intern. Conf. Phys. on Semicond. San Francisco (Springer, New York 1984) p. 1321
48. P.W. Bridgeman: Proc. Natl. Acad. Sci. USA **21**, 109 (1935)
49. M. Okajima, S. Endo, Y. Akahama, S. Narita: Jpn. J. Appl. Phys. **23**, 15 (1984)
50. Y. Akahama, S. Endo, S. Narita: Proc. 10th AIRAPT Intern. High Pressure Conf., Amsterdam (1985) (to be appeared)
51. I.V. Berman, N.B. Brandt: Zh.ETF Pisma **7**, 412 (1968)
52. J. Wittig, B.T. Mathias: Science **160**, 994 (1968)
53. H. Kawamura, K. Tachikawa, R. Shimomura, I. Shirotani: Kotai Butsuri **19**, 693 (1984) (in Japanese)
54. H. Kawamura, I. Shirotani, K. Tachikawa: Physics Monthly (in Japanese) **6**, 409 (1985)
55. H. Fukuyama: J. Phys. Soc. Jpn. **51**, 1709 (1982)